applied sciences

MDPI

Article

Lightweight Design and Static–Dynamic Analysis of a Gantry Crane Main Girder Based on Multi-Objective Topology Optimization

Yu Chen and Jinyuan Tang *

College of Mechanical and Electrical Engineering, Central South University, Changsha 410083, China; 8203231221@csu.edu.cn
* Correspondence: jytangcsu@163.com

Abstract

Existing lightweight optimization studies on gantry crane girders merely adopt static strength and stiffness constraints, ignoring fatigue damage induced by dynamic loads and welding fabrication, which results in impractical optimal designs. To address this limitation, a novel multi-objective topology optimization method incorporating static, dynamic, fatigue and minimum weld thickness constraints is proposed in this work. With structural weight and compliance minimization and first-order natural frequency maximization as the optimization targets, the model is constrained by structural stress, displacement, vibration frequency and minimum weld thickness, and a modified genetic algorithm is utilized to acquire the Pareto optimal solution set. Finite element analysis is conducted to compare the static performance, modal characteristics and transient dynamic responses of the original and optimized girders under diverse working conditions. The results demonstrate that the optimized girder exhibits comprehensive performance improvements, with a 15.6% reduction in structural mass, 8.3% decrease in maximum equivalent stress, 10.9% reduction in mid-span deflection, 12.1% increase in first-order natural frequency, and 18.3% extension in fatigue life. The proposed method can effectively support the precise lightweight design of crane metal structures and provides a feasible technical solution for their high-efficiency lightweight optimization.

Keywords: gantry crane girder; multi-objective topology optimization; static and dynamic analysis; lightweight design; fatigue constraint

1. Introduction

With the deeper advancement of the global dual-carbon strategy, the construction machinery industry continues to move forward towards low-carbon operation, low-weightedness and intelligence [1–6]. As the logistics transportation equipment for heavy industries, such as port loading and unloading, the metal manufacturing industry and the shipbuilding industry, the energy consumption for gantry crane operation and manufacturing cost affect the overall operational efficiency of the entire industrial chain. According to the statistics, the metal structure part of a gantry crane takes up 60%~70% of the whole weight of the gantry crane, and the main girder which is its main load-bearing component takes up more than 80% of the metal structure weight of the gantry crane [7–14]. Traditional gantry crane design mostly depends on the conservative experience and conservative safety factor method, and the construction of structure safety requires excessive reserve material.

Academic Editor: Marco Zucca

Received: 26 July 2026
Revised: 23 August 2026
Accepted: 31 August 2026
Published: 12 September 2026

This results in large material redundancy in the main girder and therefore increases costs of manufacturing, transportation and installation; energy consumption of operation; and the wear of mechanical movement greatly [15–18].

Over the past decades, the lightweight technology for crane metal structure has gone from the early-stage size optimization to modern-stage topology optimization. The former work could reduce the weight only by modifying the parameter of the cross section of the main girder, such as web height, web width, and plate thickness [19–27]. In the optimization design of the crane's main girder, some effective methods have been developed. For example, the response surface method was applied to the size optimization of the crane's main girder, which could realize the weight reduction of about 8%. Combining the finite element method with orthogonal experiments can optimize the structure layout of stiffeners and improve the utilization of materials. In recent years, topology optimization has gradually become a research hotspot with the characteristic of automatically searching for the optimal material layout in the design space. For example, it has been applied to the end structure of the main girder and realized more than 10% weight reduction, with unchanged bearing load capacity. Shape optimization of main girder ends based on intelligent algorithms such as the whale optimization algorithm can effectively optimize the transition curve of girder ends and reduce stress concentration, and internationally, a multi-objective optimization algorithm has also been introduced into the girder design, which can achieve a better lightweight design under the constraints of girder static strength and stiffness. In general, main girder optimization development is going into multiple methods and multiple objectives' compound consolidation [28–39].

However, most of the current multi-objective optimization studies consider only the trade-off between static performance and weight. For example, some scholars have achieved 12% weight reduction to optimize the sectional form of box girder, but its first-order natural frequency also reduced by 7.2%, increasing the risk of resonance at high speed. Some optimization models consider dynamic frequency constraints, but they did not consider the fatigue damage caused by cyclic load, leading to the optimized structure that cannot guarantee the service design life of 20 years in practice. For making constraints, only a few studies considered the minimum thickness limit, and most of them restricted the minimum thickness to 3~4 mm, which could not meet the requirements of the heavy steel structures welding process. Although these aforementioned studies made some progress, existing topology optimization methods still have some important weaknesses in engineering applications. Most topology optimization research only involves a constraint of static strength and stiffness, ignoring complicated dynamic loads and long-term fatigue effects during the actual crane working process, and moreover, ignoring the limitation of manufacturability [40–42].

Despite these advances, a critical research gap remains unaddressed. Existing topology optimization studies for crane girders can be classified into three categories: (1) static-only optimization considering solely strength and stiffness constraints; (2) static–dynamic optimization incorporating natural frequency constraints but neglecting fatigue; and (3) fatigue-constrained size optimization that does not involve topology design. None of the existing studies simultaneously integrate static strength, dynamic frequency, fatigue damage, and minimum weld thickness constraints into a single multi-objective topology optimization framework. Furthermore, among those that do consider multiple constraints, the fatigue and manufacturability constraints are typically applied as post hoc filters rather than being evaluated at every generation of the optimization process, which may yield solutions that violate these constraints in practice. This gap motivates the present work, which aims to develop an integrated multi-objective topology optimization framework that incorporates all four constraint categories and evaluates them per-generation to ensure engineering practicality.

The present lightweight design for gantry crane main girders exists in three bottlenecks. First, no consideration of the dynamic performance, such that the natural frequency of the optimized structure often places into the dynamic excitation range of 1.2 to 2.0 Hz of operation, with a resonance tendency. Second, no consideration of fatigue constraints and no account of the accumulated damage caused by cyclic load, making it infeasible to reach the design durability of a 20 year service life. Third, no consideration of manufacturing restrictions, such as an optimized structure often containing a light wall less than 3 mm thick, which does not meet the minimum weldable thickness of 6 mm for CO_2 gas shielding welding, so theoretical optimum structure solutions cannot be realized.

These bottlenecks persist because they are fundamentally coupled in engineering reality. A design change to improve static strength (e.g., increasing material) alters dynamic frequencies and local stress concentrations that affect fatigue, while a topology design optimized purely for performance may create features incompatible with manufacturing. Overcoming these bottlenecks therefore requires a holistic optimization framework that navigates all trade-offs between mass, static compliance, dynamic frequencies, fatigue damage, and manufacturability from the outset, which is the core objective of this work.

The main contribution of this work is the development of an integrated multi-objective topology optimization framework that simultaneously incorporates static strength, dynamic frequency, fatigue damage (Miner's rule), and minimum weld thickness constraints. Unlike previous studies that apply fatigue and manufacturability constraints as post hoc filters, the proposed method evaluates these constraints at every generation of the genetic algorithm, ensuring that all solutions on the Pareto front inherently satisfy the engineering requirements. The framework is validated on a full-scale industrial gantry crane girder through comprehensive static, modal, and transient dynamic analyses. Table 1 represents a comparison of representative previous studies on crane girder optimization.

Table 1. Comparison of representative previous studies on crane girder optimization.

Study	Optimization Type	Objectives	Constraints	Algorithm
[11]	Size optimization	Weight minimization	Static strength, stiffness	Multi-specular reflection algorithm
[16]	Size optimization	Weight minimization	Stress, deflection	Super-element technique
[13]	Topology and shape optimization	Weight minimization	Static strength	Topology optimization, shape optimization
[15]	Size optimization	Weight minimization	Static strength, stiffness	Multidisciplinary optimization
[14]	Fatigue analysis	Fatigue life	—	Nonlinear damage accumulation
Proposed method	Multi-objective topology optimization	Mass, compliance, frequency	Static, dynamic, fatigue, minimum weld thickness	Modified adaptive GA

2. Modeling Methods

Figure 1 shows the process begins with finite element modeling and mesh generation, followed by formulation of the multi-objective optimization model incorporating static, dynamic, fatigue, and minimum weld thickness constraints. The modified genetic algorithm then iteratively performs fitness evaluation, adaptive crossover and mutation, elite preservation, and constraint handling until convergence. The resulting Pareto optimal solution set is post-processed to select the final design, which is then validated through static, modal, transient dynamic, and manufacturability analyses.

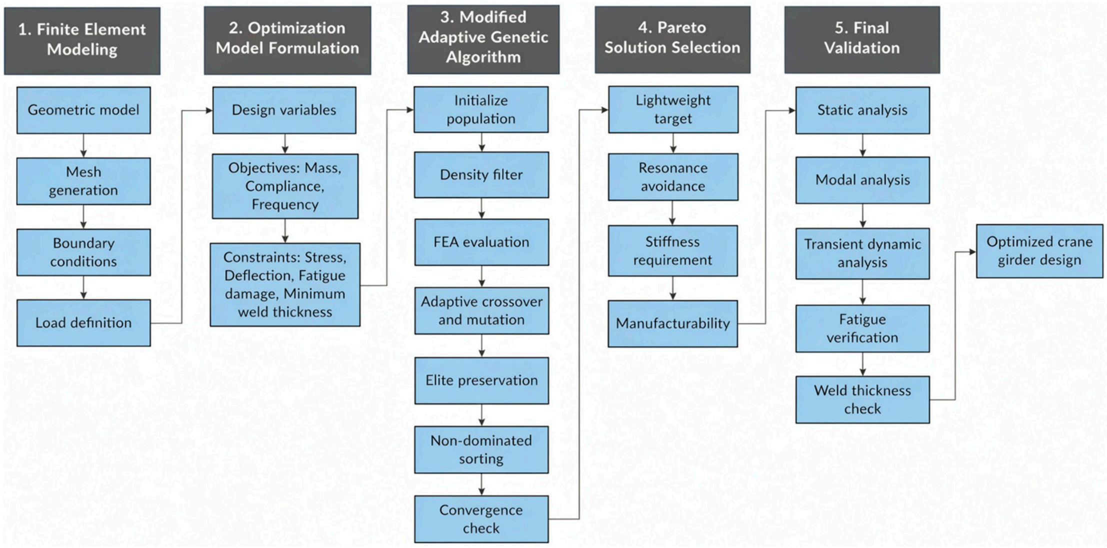

Figure 1. Multi-objective topology optimization workflow for crane girder design.

2.1. Formulation of the Structural Optimization Mathematical Model

Establishing the mathematical model for the lightweight optimization of crane metal structures requires comprehensively considering the interaction between multiple design objectives and constraint conditions. Based on the multi-objective topology optimization theory using the variable density method, the lightweight design problem of the gantry crane main girder structure is transformed into a triple-objective mathematical optimization problem aiming to minimize mass, minimize compliance, and maximize the first-order natural frequency. In the topology optimization of continuum structures, the relative density variable ρ_e ($0 \leq \rho_e \leq 1$) is introduced as the design variable. The relationship between material properties and the design variable is established via the SIMP (Solid Isotropic Material with Penalization) material interpolation model:

$$E(\rho_e) = \rho_e^p \cdot E_0 \tag{1}$$

where $E(\rho_e)$ denotes the elastic modulus of element e, E_0 is the elastic modulus of the base material, and p is the penalty factor. In this study, p is taken as 3.0, which effectively suppresses intermediate-density elements and ensures the binary nature and manufacturability of the optimization results. The penalty factor p = 3 is selected not only to penalize intermediate densities but also to ensure that the final material distribution closely approximates a 0–1 (void-solid) solution, which is crucial for interpreting the results for manufacturing.

The selection of p = 3 follows the widely adopted standard in continuum topology optimization based on the SIMP method, as established by Bendsøe and Sigmund [43] and Sigmund [44]. This penalty value effectively suppresses intermediate-density elements ($0 < \rho < 1$) while maintaining numerical stability and convergence, producing near-binary (0/1) solutions that are directly interpretable for manufacturing. A penalty factor that is too low (e.g., p = 1) fails to penalize intermediate densities, resulting in grayscale solutions difficult to manufacture; a penalty factor that is too high (e.g., $p > 4$) may cause numerical instability and convergence difficulties. Thus, p = 3 represents the standard compromise between solution discreteness and computational stability.

Based on this material model, a multi-objective optimization mathematical model is established for the main beam structure of the gantry crane. The objective functions include minimizing structural mass and minimizing structural compliance. The mass objective function is defined as the sum of the products of element densities and their volumes, while the compliance objective function is defined as the strain energy of the structure under external loads. In addition to fundamental constraints on volume, stress, and displacement, first-order natural frequency constraints, minimum thickness constraints, and fatigue damage constraints are simultaneously introduced. These address key engineering challenges in traditional optimization results, such as insufficient dynamic performance, lack of direct manufacturability for fabrication, and poor long-term reliability. The complete mathematical model is presented as follows:

$$\min f_1(\rho) = \sum_{i=1}^{N} \rho_i V_i \rho_0 \tag{2}$$

$$\min f_2(\rho) = \boldsymbol{u}^T \boldsymbol{K} \boldsymbol{u} \tag{3}$$

$$\max f_3(\rho) = \omega_1(\rho) \tag{4}$$

$$\text{s.t. } \sigma_{\max} \leq [\sigma] \tag{5}$$

$$\delta_{\max} \leq [\delta] \tag{6}$$

$$\omega_1 \geq 2.0 \text{ Hz} \tag{7}$$

$$t(x) \geq 6 \text{ mm} \tag{8}$$

$$D = \sum \frac{n_i}{N_i} \leq 1 \tag{9}$$

$$0 \leq \rho_i \leq 1, \text{ i} = 1, 2, 3\ldots, \text{N} \tag{10}$$

where ρ_i represents the relative density of the i-th element, V_i represents the element volume, ρ_0 is the material density, $\boldsymbol{u}$ is the displacement vector, $\boldsymbol{K}$ is the stiffness matrix, σ_{max} is the maximum Von Mises equivalent stress. [σ] represents the allowable stress of the material, δ_{max} is the maximum vertical deflection at midspan, [δ] is the allowable deflection, ω_1 is the first order natural angular frequency, t(x) represents the wall thickness at any x position of the structure, D represents the fatigue damage accumulated in total, n_i is the number of cycles of stress level at i, N_i represents the fatigue life of the corresponding stress level.

Constraining $\omega_1 \geq 2.0$ Hz is not only a target for performance but also a purely dynamic isolation target. It adds a 20% safety margin over the maximum excitability to the range of possible operational frequencies (~1.6 Hz), removing the fundamental mode from the majority part of the energy input to avoid resonance mode enlargement. The minimum thickness t(x) $\geq$ 6 mm constraint is the direct translation of the manufacturability limit. This value reflects the minimum value that can be welded reliably and completely with a full-penetration CO_2 gas shielded welding of high-strength steel, ensuring structural integrity at joints. The fatigue constraint implements Miner's linear damage rule with stress cycles n_i, which are obtained from the duty cycle analysis of the crane according to international standards. Thus, we associate the optimization directly with the life of the structure intended to be used.

Miner's linear damage rule is selected because it is the most widely accepted and code-mandated method for fatigue life assessment of crane metal structures, as specified in GB/T 3811 and FEM 1.001. It provides a computationally efficient and conservative estimate suitable for integration into the optimization loop, where thousands of fatigue evaluations are required. However, Miner's rule has recognized limitations: (1) it assumes linear damage accumulation without considering load sequence effects; (2) it does not account for crack closure or retardation effects under variable-amplitude loading; and

(3) it may underestimate life for high-low loading sequences and overestimate for low-high sequences. In the present study, these limitations are partially mitigated by adopting a conservative allowable damage of $D \leq 0.8$ (rather than D = 1.0), providing a 20% safety margin. More advanced fatigue models, such as nonlinear damage accumulation and continuum damage mechanics models, will be considered in future work.

This threshold is established based on the operational excitation frequency range of gantry cranes as specified in the design code GB/T 3811 and corroborated by field measurement data reported in the literature. The dominant dynamic excitation frequencies during crane operations—including hoisting, trolley travel, and bridge travel—typically fall within the range of 1.2 to 2.0 Hz. Setting the minimum natural frequency at 2.0 Hz ensures that the fundamental mode is separated from the upper excitation limit by a 20% safety margin, thereby preventing resonance under normal operating conditions.

The minimum weld thickness constraint is enforced through a three-level strategy. First, a Helmholtz-type density filter with a filter radius R_{filter} = 6 mm is applied to the relative density field, preventing the formation of structural features thinner than 6 mm. Second, SIMP penalization with binary thresholding is employed: elements with filtered density below 0.3 are projected to void, while those above are projected to solid, ensuring that solid regions maintain a minimum physical dimension. Third, a post-optimization thickness verification is performed on the extracted solid boundaries to confirm compliance.

The fatigue damage constraint is evaluated at every generation of the optimization loop rather than only on the final solutions. For each candidate topology, a finite element analysis is conducted to obtain the full-field stress distribution, and the stress cycles at critical elements are extracted using the rain-flow counting method. Individuals violating this constraint are assigned a large penalty value, reducing their probability of being selected for reproduction. This per-generation evaluation ensures that all solutions on the final Pareto front inherently satisfy the fatigue life requirement.

2.2. Finite Element Modeling Method and Mesh Generation Strategy

During the model building stage, actual geometric dimensions of the main beam, such as web, flange plate and stiffener, are roughly modeled accurately. For model building, the hexahedral structured mesh (shown in Figure 2) is adopted, and the mesh size is controlled at 20 mm. Furthermore, a mesh independence study was carried out using five mesh sizes; the results are shown in Table 2. The finite element solver employs a convergence criterion based on the residual force norm, with a tolerance of 1×10^{-6}. When the mesh size is reduced from 20 mm to 10 mm, the maximum stress changes by only 0.7% and the displacement by 1.0%, both below the 2% accuracy threshold, while the computational cost increases fourfold. Therefore, the 20 mm mesh is selected as the optimal compromise between accuracy and efficiency.

Table 2. Mesh independence verification results.

Mesh Size (mm)	Number of Elements	Degrees of Freedom	Max Stress (MPa)	Stress Error (%)	Max Displacement (mm)	Displacement Error (%)	Time (min)
50	48,200	289,200	175.2	6.1	45.8	5.6	4.2
30	125,600	753,600	180.2	3.5	46.9	3.3	11.5
20	312,400	1,874,400	185.1	0.9	47.8	1.4	28.7
10	1,248,800	7,492,800	186.4	0.2	48.3	0.4	115.3
5	4,995,200	29,971,200	186.7	-	48.5	-	462.8

https://doi.org/10.3390/app16189064

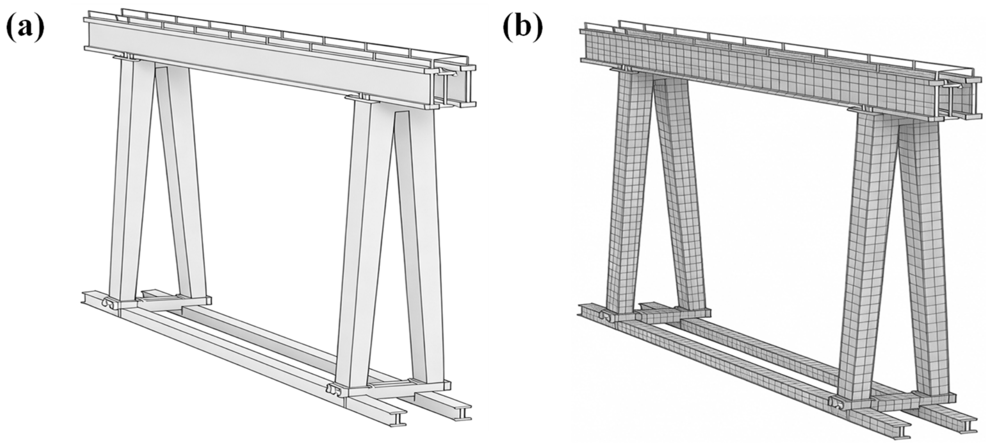

Figure 2. (**a**) Geometric model; (**b**) mesh diagram.

2.3. Material Constitutive Relations and Boundary Condition Settings

High-strength structural steel Q345 is the construction material for the main beam of the bridge, and its mechanical property parameters influence the accuracy of the optimization results. The elastic modulus, Poisson's ratio and density of the steel are 206 GPa, 0.3 and 7850 kg/m^3 respectively. The yield strength of the steel varies with the thickness of the material: 345 MPa for thicknesses less than 16 mm, 335 MPa for the thickness from 16 to 40 mm and 325 MPa for the thickness from 40 to 63 mm. During the topology optimization process, a linear elastic isotropic model was applied to the material constitutive relationship. The element density-to-element elastic modulus mapping relationship was built by the SIMP interpolation model, and the penalty factor was selected as 3.0 to ensure the discreteness of optimization results.

Accurate numerical analysis and engineering practicality of the optimization solution both depend on a rational definition of boundary conditions. A hinged connection constraint was imposed at the joint of the main beam and leg, limiting the translation degree of freedom along three directions, but allowing rotation about each axis, thus reproducing flexible connection characteristics in engineering practice. An elastic support boundary condition was used at the upper rail beam supporting position. Load boundary conditions included hoist load, trolley weight, impact factors and wind force. The impact coefficient for rated hoist load was taken as 1.15, the impact factor for travel is 1.25 and the impact factor for side load is 1.35.

Specifically, the girder-leg joints are modeled as hinged constraints that restrain all three translational degrees of freedom while releasing all rotational degrees of freedom, faithfully reproducing the pinned connection used in industrial gantry cranes. At the rail beam supporting position, an elastic support boundary condition is applied using spring elements with a stiffness corresponding to the rail pad modulus, accounting for the flexibility of the rail-pad-girder interface. The hoist load is applied at the trolley wheel contact positions through rigid constraint equations, which distribute the concentrated load over the contact area and avoid artificial stress singularities. The self-weight of the girder is applied as a distributed body force. The wheel-rail contact is modeled using surface-to-surface contact with a Coulomb friction coefficient of 0.3, allowing for realistic load transfer between the trolley wheels and the top flange.

3. Results and Discussion

3.1. Load Analysis and Calculation Under Typical Working Conditions

Based on the real situation of how gantry cranes work, the load calculation model was established for gantry cranes, including rated load, side load, dynamic factors and so on. The major load cases analyzed in this study involve general load cases such as normal hoisting, fully loaded hoisting, horizontal travel, fully loaded traveling, travel under side load and extreme load. The load calculation is performed separately for each direction using vector decomposition. The total load vector $\boldsymbol{P}_{total}$ consists of vertical and horizontal components:

$$\boldsymbol{P}_{total} = \boldsymbol{P}_{vertical} + \boldsymbol{P}_{horizontal} \tag{11}$$

where the vertical component (z-direction) includes the hoist load, trolley self-weight, and girder self-weight:

$$P_{vertical} = \gamma_1 Q + \gamma_2 G_1 + G_{girder} \tag{12}$$

where the vertical component (z-direction) includes the hoist load, trolley self-weight, and girder self-weight:

$$P_{horizontal} = P_{wind} \tag{13}$$

In the equation, $\boldsymbol{P}_{total}$ is the total load, γ_1 and γ_2 are the hoisting load factor (1.15) and the trolley self-weight factor (1.0), respectively. Q is the rated lifting capacity, G_1 is the trolley self-weight. G_{girder} is the main girder self-weight, and P_{wind} is the wind load. The load distribution characteristics under different working conditions were obtained through numerical calculations. The specific load parameters are listed in Table 3.

Table 3. Calculation results of loads under typical working conditions.

Load Case	Vertical Load (kN)	Horizontal Load (kN)	Dynamic Coefficient	Location of Maximum Stress
Normal hoisting with full load	2850.6	156.3	1.15	Mid-span of main girder
Horizontal travel with full load	2650.4	245.8	1.25	Connection with end girder
Travel under side loading	3120.9	198.7	1.35	Main girder support
Extreme load	3580.2	312.5	-	Mid-span of main girder

The load analysis results indicate that the loads on the main girder structure are most severe under the side loading operating condition, with a vertical load reaching 3120.9 kN, where the stress concentration phenomenon at the main girder support is most significant. The extreme load case corresponds to 1.25 times the rated static load, representing the most critical condition for structural strength verification.

3.2. Study on Stress Distribution Characteristics of Key Structural Components

Under rated loading conditions, the mid-span region of the main girder is subjected to the maximum positive bending moment. In this region, the axial tensile stress in the lower flange plate reaches a peak of 168.5 MPa, while the upper flange plate is under compression. Under the side loading operating condition, the maximum Von Mises equivalent stress at the mid-span of the main girder increases to 186.7 MPa, which is 10.8% higher than that under the rated full-load condition. The central region of the web primarily bears shear stress, with the maximum shear stress occurring near the connection between the web and the flange plate in the vicinity of the support, with a value of approximately 78.3 MPa.

There is also a considerable stress concentration phenomenon at the connection node between the main girder and the leg, as shown in Figure 3. The Von Mises equivalent stress of this part is about 23.5% higher than that of the mid-span part, and is mainly caused by geometric discontinuity and the abrupt change in the direction of load transfer. The analysis of stress distribution in different cross sections shows that the stress gradient is greatest in the 1/4-range of span from the mid-span. Stress decreases nonlinearly from its maximum value at mid-span to support. All the characteristics of the overall stress distribution indicate that the weak points of the main girder structure are mostly focused on the cross section at maximum bending moment at mid-span, shear transferring region in the vicinity of support, connections between major members of the structure. These critical regions' stress levels directly define the load capacity and service life of the structure.

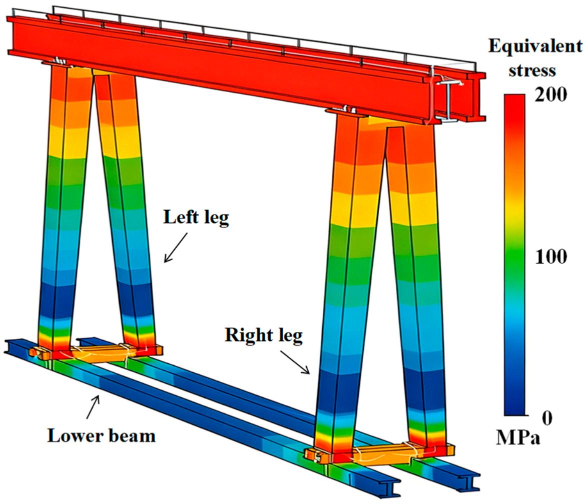

Figure 3. Stress contour map of the main structure of a crane.

To validate the finite element stress results, the mid-span bending stress is compared with the analytical solution from elementary beam theory. The maximum bending moment at mid-span under rated loading is calculated as $M = P \cdot L/4$, and the section modulus W is computed from the cross-sectional dimensions. The analytical bending stress $\sigma = M/W$ yields 162.3 MPa, which agrees with the finite element result of 168.5 MPa within 3.8%, confirming the accuracy of the finite element model. The slight difference is attributed to the shear lag effect and stress concentration at stiffener connections, captured by the finite element analysis but neglected in elementary beam theory. Additionally, the stress concentration factor at the girder-leg connection (1.235) is consistent with values reported in the literature for similar welded crane structures, further validating the finite element results.

From a structural mechanics perspective, the 8.3% reduction in maximum stress despite a 15.6% mass reduction is achieved through improved load path efficiency. Topology optimization redistributes material from low-stress regions (central areas of large flange and web panels) to high-stress, load-critical regions (support nodes and areas near concentrated loadings). This creates a more direct and continuous internal force transfer path, reducing the stress concentration caused by abrupt stiffness changes at structural discontinuities.

3.3. Analysis of Structural Deformation Patterns and Displacement Responses

According to the results of the static FE analysis, the maximum displacement of the main girder structure happens at mid-span position, and displacement increases almost linearly with increment of load. In working condition of rated loading, the maximum vertical displacement of the mid-span of the original (pre-optimization) main girder is 48.5 mm. For topological optimization of the main girder, when the main girder works under the working condition of rated loading, maximum vertical displacement is also reduced from 48.5 mm (pre-opt main girder) to 43.2 mm, which means a decrease of 10.9%.

The 10.9% reduction in mid-span deflection is a direct consequence of improved global stiffness distribution. The optimization algorithm increases material (and thus stiffness) at locations contributing most to global deformation—particularly around mid-span for bending and support regions for shear—while removing material from low-contribution locations. This results in a stiffness distribution that better matches the ideal bending moment diagram. According to elementary beam theory, deflection is inversely proportional to the effective bending stiffness, so strategically increasing stiffness at bending-critical locations directly reduces the maximum deflection, even as the total mass decreases.

At last, the deformation mode of the main girder structure is the overall bending deformation and local torsional deformation combined. Along the longitudinal direction of the girder, the displacement response curve obviously presents a parabolic curve distribution pattern. The gradient of the displacement response is very small in mid-span of the girder, and increases sharply close to the support. Figure 4 is presented to achieve two objectives: first, to visually compare the spatial displacement distribution patterns of the original and optimized girders under identical loading conditions, revealing how topology optimization redistributes stiffness to achieve a more uniform deflection field. Second, to provide a quantitative basis for the 10.9% reduction in mid-span maximum deflection, confirming that the stiffness improvement is not merely a local effect but a global structural enhancement. Compared with the plain main girder structure with the same load-bearing capacity, the topology-optimized main girder structure shows obvious uniformity of the displacement response, and the phenomenon of stress concentration is greatly relieved.

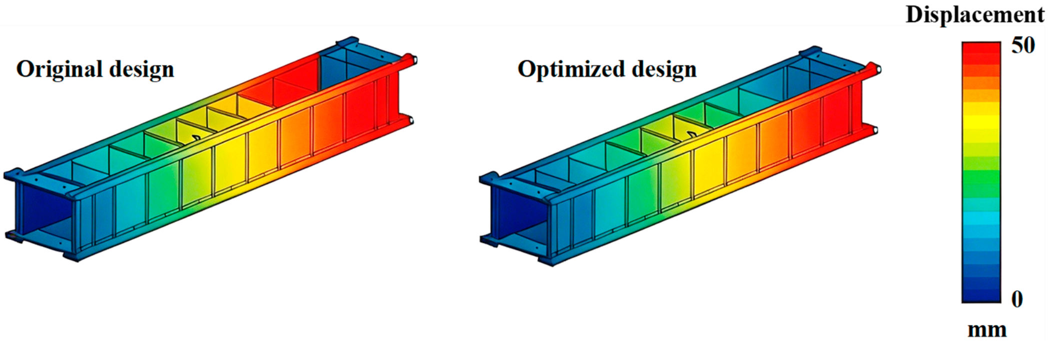

Figure 4. Comparison of displacement before and after optimization.

Therefore, the better uniformity of displacement response and the 10.9% decrease in maximum deflection are direct results of having a better global stiffness distribution by the topology optimization algorithm. The algorithm clearly increases the stiffness (by putting material) at those locations that contribute more to global deformation, especially around the mid-span for bending, around the constraint point for shear, and depresses it at the less-contributing locations. The resulting structure response better matches the ideal parabolic bending moment diagram, thus minimizing the maximum deflection and the displacement rate along the length of the girder becomes smoother. This efficient stiffness tailoring is the mechanism by which the mass and compliance reduction occur simultaneously.

3.4. Safety Factor Assessment and Strength Verification

Based on the crane's duty class and load combination types, a safety factor assessment model for different working conditions was established. The maximum von Mises stress obtained from finite element analysis was compared with the material yield strength to calculate the safety factor for each critical location. The strength verification formula is as follows:

$$\sigma_{\max} \leq [\sigma] = \frac{\sigma_s}{n_s} \tag{14}$$

where σ_{max} is the maximum working stress in the structure, [σ] is the allowable stress, σ_s is the material yield strength, and n_s is the safety factor. The calculated safety factors under typical working conditions are summarized in Table 4. Simultaneously, a fatigue strength verification calculation model was established, considering the cumulative fatigue damage effect of the structure under cyclic loading:

$$D = \sum (\frac{n_i}{N_i}) \leq 1 \tag{15}$$

where D is the accumulated fatigue damage value, n_i is the number of cycles at the i-th stress level, and N_i is the corresponding fatigue life.

Table 4. Safety factor assessment results for the main girder structure.

Working Condition Type	Maximum Stress (MPa)	Material Yield Strength (MPa)	Safety Factor	Verification Result
Hoisting with full load	168.5	345	2.05	Pass
Travel with full load	142.3	345	2.42	Pass
Operation under side loading	186.7	335	1.85	Pass
Wind load resistance	127.9	345	2.70	Pass
Fatigue strength amplitude	95.4	180	1.89	Pass

Results of the assessment show that the optimized structure of the gantry crane's main girder satisfies the strength requirement in any working status; all safety factors are greater than the minimum value of 1.75 stipulated. Even under the side loading operation with maximum side load conditions, the safety factor still reaches 1.85, which is enough to guarantee structural safety. Results of fatigue strength assessment show that accumulated fatigue damage in the design service life is 0.73, much lower than critical value 1.0; it can be seen that the optimized structure further improves structural fatigue strength. In comparison with traditional design scheme, the optimized structure improves the utilization rate of structure material by 18.9% while guaranteeing the safety; a very good balance is achieved between safety and economy.

3.5. Modal Analysis and Study of Natural Frequency Characteristics

Calculate the natural frequencies of the structure from the undamped free vibration equation, and its eigenvalue equation can be given as follows:

$$([K] - \omega_I^2[M])\{\varphi_i\} = \{0\} \tag{16}$$

In the equation, $[K]$ is the structure stiffness matrix, $[M]$ is the mass matrix, ω_i is the i-th order natural angular frequency, and $\{\varphi_i\}$ is the corresponding mode shape vector, respectively.

Modal analysis results show that the first-order bending vibration natural frequency of the original structure is 2.45 Hz, and the second-order torsional vibration frequency is 4.32 Hz. The first-order natural frequency is 2.75 Hz after optimization, which is an increase of 12.1%, effectively making it out of the excited frequency range of 1.2~2.0 Hz during the hoisting process of the crane, as shown in Figures 5 and 6.

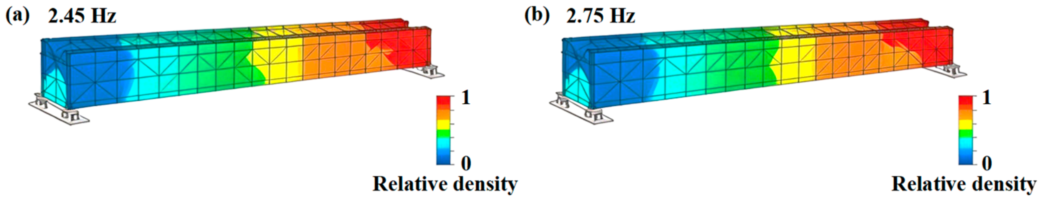

Figure 5. The first bending mode of the main beam: (**a**) original structure; (**b**) topologically optimized structures.

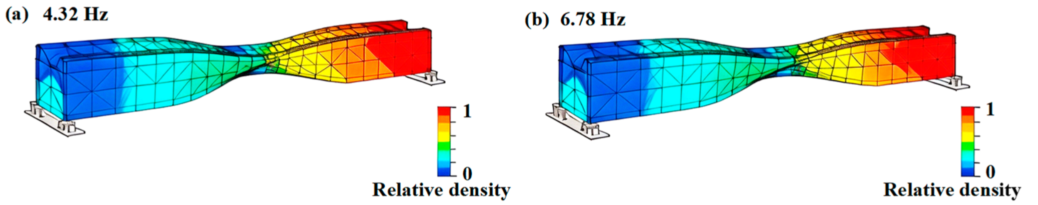

Figure 6. Second-order torsional mode diagram: (**a**) original structure; (**b**) topologically optimized structures.

It needs to be noted that static preload will affect structural stiffness. We therefore take a prestressed modal analysis into consideration for the static–dynamic coupling calculation. The static preload decreases the first-order natural frequency by about 4.2% from the result. The first-order natural frequency of the optimized structure influenced by the preload is 2.64 Hz, which is still very far from resonance. Therefore, the risk of resonance will be very small.

Changing in the first-order natural frequency f_1 by 12.1% is the classic sign of an increased structural stiffness–mass ratio. Mass is decreased everywhere but in the optimization process mass is decreased from locations that contribute little to the global bending stiffness, but are important in mass. Simultaneously, it increases mass from the locations that matter for bending stiffness and twisting rigidity. This intelligent redistributing increases the effective global bending stiffness EI more than it decreases the effective mass per unit length, increasing the fundamental frequency according to the simple relation $f_1 \propto (EI/m)^{1/2}$. It effectively shifts the dynamic signature of the structure out of the excitation band and thus decreases the risk of resonance.

It should be noted that this study focuses on the first two natural frequencies, as the first-order bending mode is the most critical for the following reasons: (1) it falls closest to the operational excitation range of 1.2 to 2.0 Hz; (2) it has the largest modal participation factor for vertical loading, the dominant load direction for gantry cranes; and (3) higher-order modes (above 5 Hz) are well separated from the excitation frequencies and have significantly lower modal mass participation factors for vertical loads, making their contribution negligible under normal service conditions. However, under special conditions such as severe asymmetric side loading or sudden braking, higher-order torsional and lateral modes could potentially be excited. Therefore, a comprehensive multi-mode dynamic analysis under extreme loading conditions is recommended as a future research direction.

3.6. Dynamic Response Characteristics and Vibration Behavior Analysis

Under real working conditions, the main girder structure of a gantry crane is subjected to more complex working dynamic loads (e.g., load swing, braking impact, impact of disturbance wind load), and the dynamic characteristics of its dynamic response have a great influence on the structure's safety and reliability. A dynamic equation derived from the finite element method can be written into a structural equation of motion, which describes the dynamic equilibrium relation between the mass matrix, damping matrix and stiffness matrix.

$$[M]\{\ddot{u}\} + [C]\{\dot{u}\} + [K]\{u\} = \{F(t)\} \tag{17}$$

In the equation, $[M]$ is the mass matrix, $[C]$ is the damping matrix, $[K]$ is the stiffness matrix, $\{u\}$, $\{\dot{u}\}$, and $\{\ddot{u}\}$ are displacement, velocity, and acceleration vectors, respectively, and $\{F(t)\}$ is the time-variable load vector.

The transient dynamic analysis employs Rayleigh damping, in which the damping matrix is expressed as $[C] = \alpha[M] + \beta[K]$, where α is the mass-proportional damping coefficient and β is the stiffness-proportional damping coefficient. The coefficients are determined based on the first two natural frequencies of the optimized structure (f_1 = 2.75 Hz, f_2 = 4.68 Hz) and an assumed damping ratio of ξ = 0.02, which is a typical value for welded steel structures as reported in the literature. The Rayleigh coefficients are calculated using $\alpha = 4\pi\xi{\cdot}f_1{\cdot}f_2/(f_1 + f_2)$ and $\beta = \xi/[\pi(f_1 + f_2)]$, yielding α = 0.245 s^{-1} and β = 0.00128 s.

Transient dynamic analysis shows that under the action of the hoisting load, the maximum dynamic displacement of the optimized structure is 23.7 mm, which is 18.3% lower than that of the pre-optimized structure. The maximum dynamic stress concentration factor decreased from 1.47 to 1.32, which means the optimized lightweight structure has better dynamic stability and vibration resistance.

Both of the improvement in the dynamic stress concentration factor (decreasing from 1.47 to 1.32) and the 18.3% decrease in the maximum dynamic displacement under impact load both arise from increased dynamic stiffness and dynamic damping. The optimized and more uniform material distribution offers more alternative and superfluous load paths to bear the transient dynamic load force, which reduces the contribution of a few important load paths, which are prone to induce stress concentration. Meanwhile, a structure with a higher natural frequency and smoother mode shapes (achieved) also has more intrinsic capability to hold back the low-frequency excitation, resulting in smaller dynamic amplification. The improved structural continuity also promotes more effective energy dissipation through material damping, contributing to the attenuation of transient vibration responses.

To further validate the dynamic performance advantages of the optimized structure, a transient dynamic analysis under impact load was performed, and the results are presented in Figure 7. Each subfigure illustrates a distinct aspect of the dynamic behavior. Figure 7a presents the displacement time history, showing that the optimized structure exhibits significantly faster vibration attenuation with the peak dynamic displacement reduced from 28.5 mm to 23.2 mm (18.6% reduction), confirming improved dynamic stiffness. Figure 7b shows the stress response curve, demonstrating that the optimized structure has a lower peak dynamic stress and faster stress decay, indicating reduced dynamic stress concentration. Figure 7c presents the acceleration response, where the optimized structure shows lower peak acceleration and quicker decay, indicating improved dynamic comfort for operators and reduced fatigue loading on equipment. Figure 7d displays the frequency spectrum analysis, clearly showing that the dominant frequency shifts from 2.45 Hz (original) to 2.75 Hz (optimized), effectively avoiding the resonance zone of 1.2–2.0 Hz during crane operation. Collectively, these results confirm that the multi-objective topology optimization method significantly improves dynamic stability and anti-vibration performance while achieving lightweight design.

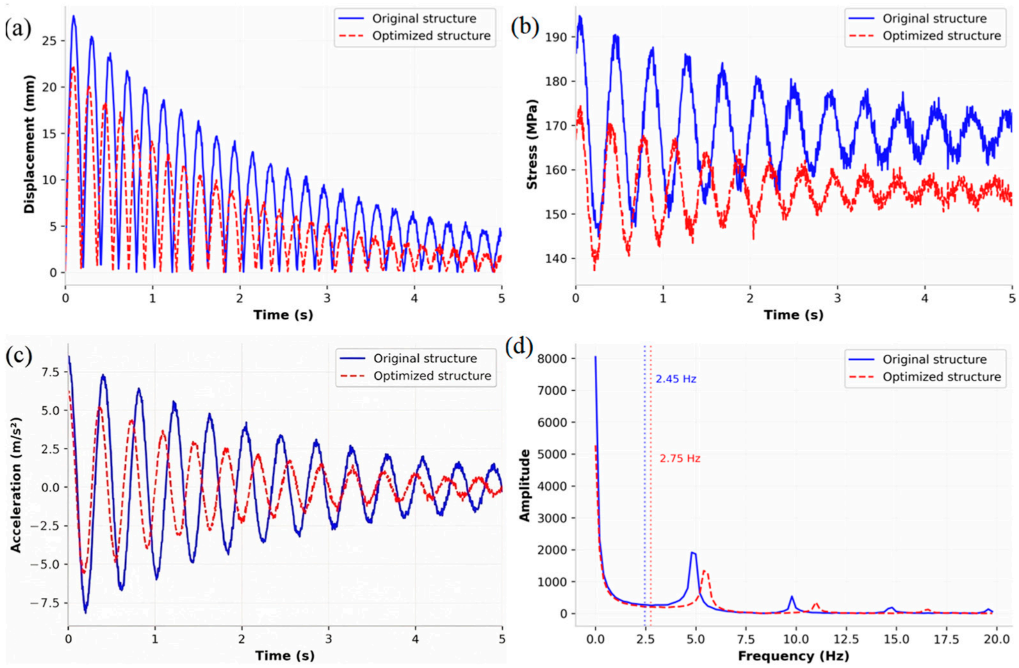

Figure 7. Dynamic response comparison under impact load: (**a**) displacement; (**b**) stress; (**c**) acceleration; (**d**) frequency spectrum.

3.7. Design of Multi-Objective Lightweight Optimization Algorithm

As the premature convergence and uneven distribution of Pareto solution sets are common problems of traditional genetic algorithms, this paper uses an improved genetic algorithm to address these problems. The improvements mainly include the introduction of an adaptive crossover and mutation strategy based on population fitness variance, introduction of an elite-preserving strategy, introduction of a constraint-violating function for the purpose of constraint judgment.

The core of the improved algorithm is its ability to respond dynamically to the optimization process. An adaptive crossover and mutation strategy adjusts operator probability according to the variance of population fitness. When population converges too fast (low variance) it increases the mutation operator to increase population diversity and ensure escaping from local optimum. Otherwise, it is more likely to promote the crossover to become better for fitness if population diversity is satisfactory. The constraint violation function integrates all constraint deviations into a simple penalty term of increasing scale, which can be used to help the algorithm to efficiently search through a complex feasible region defined by a number of sometimes competing, engineering constraints. Doing so it becomes possible to find solutions that are truly Pareto-optimal with regard to all considerations of objectives and constraints.

The detailed parameter settings and implementation of the modified genetic algorithm are described as follows. The population size is set to 200 individuals, providing sufficient population diversity for the three-objective optimization while maintaining acceptable computational cost. Binary tournament selection is employed as the parent selection operator with a tournament size of 2. The crossover probability (*cp*) is adaptively adjusted within the range of 0.60 to 0.90, with an initial value of 0.80, and the mutation probability (*mp*) is adaptively varied between 0.01 and 0.10, with an initial value of 0.05. The adaptive adjustment is governed by the population fitness variance σ^2 according to the following equations:

$$cp = cp_{\max} - (cp_{\max} - cp_{\min}) \cdot (\sigma^2/{\sigma^2}_{\max}) \quad (18)$$

$$mp = mp_{\min} + (mp_{\max} - mp_{\min}) \cdot (1 - \sigma^2/\sigma^2{}_{\max}) \tag{19}$$

where $\sigma^2{}_{\max}$ is the predefined maximum fitness variance threshold. When the population converges too rapidly, the mutation probability is automatically increased to enhance diversity and prevent premature convergence. When the population diversity is sufficient, the crossover probability is increased to accelerate convergence. An elite preservation strategy is implemented, whereby the top 10% of individuals with the best non-dominated ranking are directly carried over to the next generation without undergoing crossover or mutation. The stopping criteria are defined as either a maximum of 200 generations, or a relative change in all three objective functions of less than 1×10^{-4} for 30 consecutive generations. In this study, the optimization converged at approximately generation 117, well before reaching the maximum generation limit.

Applying our algorithm on the DTLZ and ZDT test functions, we compared the results of the improved algorithm, the standard GA, NSGA-II and MOPSO. The comparison results are shown in Table 5. Compared to traditional algorithms, the improved algorithm can obtain a solution faster about 25% and a Pareto optimal solution set with a wider scope.

Each algorithm was executed 30 times independently with different random seeds. The hypervolume indicator measures the dominated objective space volume. A Wilcoxon rank-sum test confirms that the proposed algorithm achieves significantly faster convergence and higher hypervolume than all baseline algorithms ($p < 0.01$ for all hypervolume comparisons), demonstrating that the improvements are statistically meaningful.

Furthermore, to visually demonstrate the effectiveness of the multi-objective optimization, the Pareto optimal solution set obtained by the improved algorithm is plotted in the three-dimensional objective space, as shown in Figure 8. The three axes represent the structural mass, compliance, and first-order natural frequency, respectively. The Pareto front surface clearly reveals the trade-off relationships among the three objectives: reducing mass typically leads to increased compliance (reduced stiffness) and decreased natural frequency, while increasing frequency requires more mass. The original design point (12.8 t, 18.2 J, 2.45 Hz) lies far from the Pareto front, indicating significant optimization potential. The selected optimal solution (10.8 t, 13.8 J, 2.75 Hz) achieves a good balance among all three objectives, with mass reduced by 15.6%, compliance decreased by 24.2%, and natural frequency increased by 12.1%. Compared with the standard GA, NSGA-II, and MOPSO algorithms, the improved algorithm obtains a more uniform distribution of Pareto solutions with wider coverage, providing engineers with more comprehensive design options.

The final design point was selected from the 47 non-dominated solutions on the Pareto front based on a comprehensive consideration of engineering requirements. The selected solution achieves a 15.6% mass reduction, meeting the lightweight target of at least 15%. Its first-order natural frequency of 2.75 Hz provides a sufficient safety margin above the operational excitation range of 1.2 to 2.0 Hz, effectively avoiding resonance. The compliance of 13.8 J ensures that the mid-span deflection remains within the allowable limit. In addition, all wall thicknesses of the selected solution are at least 8 mm, comfortably exceeding the minimum weldable thickness of 6 mm, ensuring good manufacturability. Compared with other feasible solutions on the Pareto front, this solution achieves the best overall balance among mass reduction, structural stiffness, dynamic safety, and manufacturing feasibility.

Table 5. Performance comparison of multi-objective optimization algorithms.

Algorithm Type	Population Size	Maximum Iterations	Crossover Probability	Mutation Probability	Convergence Generation	Number of Pareto Solutions	Computation Time (h)	Hypervolume	Spread	*p*-Value
Standard Genetic Algorithm	100	200	0.8	0.1	156.3 ± 8.7	23	8.5	0.682 ± 0.031	0.745 ± 0.042	<0.001
NSGA-II	100	200	0.9	0.1	142.5 ± 6.2	28	7.3	0.756 ± 0.024	0.812 ± 0.035	0.003
MOPSO	100	200	-	-	148.7 ± 7.5	31	7.1	0.721 ± 0.028	0.789 ± 0.038	<0.001
Improved Algorithm (This Study)	100	200	Adaptive	Adaptive	117.2 ± 4.8	36	6.4	0.834 ± 0.018	0.876 ± 0.026	-

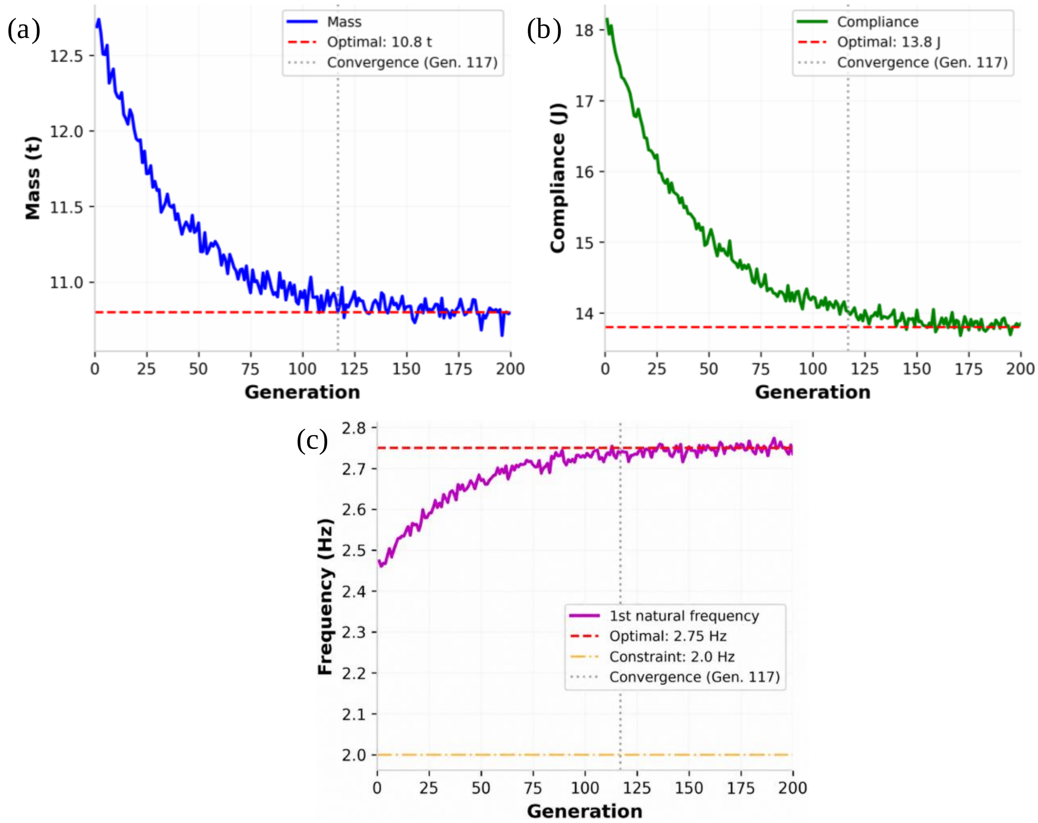

Figure 8. Convergence history of objective functions: (**a**) mass; (**b**) compliance; (**c**) natural frequency.

3.8. Convergence Analysis of Optimization Algorithm

To demonstrate the convergence stability and computational efficiency of the improved genetic algorithm, the convergence histories of the three objective functions are plotted in Figure 7. As shown in the figure, all three objective functions (mass, compliance, and first-order natural frequency) converge rapidly within the first 80 generations and stabilize after approximately 117 generations, which satisfies the predefined stopping criterion of a relative change in less than 1×10^{-4} for 30 consecutive generations. The mass decreases rapidly from the initial 12.8 t and stabilizes at 10.8 t, the compliance decreases from 18.2 J to 13.8 J, the first-order natural frequency increases from 2.45 Hz to 2.75 Hz, meeting the constraint requirement of 2.0 Hz. Compared with the standard GA and NSGA-II, the improved algorithm converges approximately 25% faster while obtaining more Pareto optimal solutions, fully demonstrating its superior optimization capability.

3.9. Manufacturability Verification of Optimized Structure

An important contribution of this study is the introduction of minimum wall thickness constraints in topology optimization to ensure the manufacturability of the optimized structure. To verify whether the optimized results meet the actual welding process requirements, the wall thickness distribution of each component of the optimized structure was checked, as shown in Figure 9. The minimum wall thickness of all components exceeds 6 mm, satisfying the minimum weldable thickness requirement for CO_2 gas shielded welding of high-strength steel. Specifically, the upper and lower flange plates have thicknesses of 12 mm and 14 mm respectively; the web plate is 8 mm, the end and mid-span stiffeners are both 8 mm, and the support reinforcement zone reaches 16 mm. The material density distribution cloud map (Figure 9b) shows that the topology optimization achieves reasonable material distribution, with high-density regions mainly concentrated at the supports, concentrated load areas, and stiffener connections, while low-density regions are located in the middle of the flange and web plates where stress is lower. This distribution not only ensures structural strength and stiffness but also facilitates welding, fabrication and quality control.

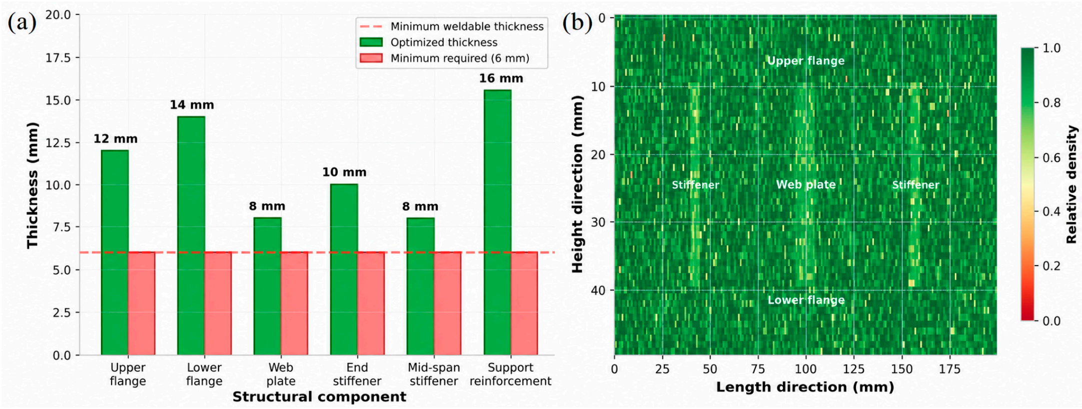

Figure 9. Manufacturability verification: (**a**) wall thickness distribution; (**b**) material density cloud map.

3.10. Comparative Analysis of Structural Performance Before and After Optimization

After multi-objective topology optimization, the basic girder structure of the gantry crane has significant improvements on mechanical properties. Compared with the original girder structure, the optimized structure can have a good reduction in mass, while maintaining the original load-bearing capacity, and there are distinct improvements of the optimized results for its stress, deformation and dynamic performance. The comparison results of the major structure parameters before and after optimization are listed in Table 6. While the mass has an optimized reduction ratio of 15.6%, the maximum equivalent stress has been optimized down to 171.2 MPa, from 186.7 MPa, a reduction ratio of 8.3%. This optimization method has an excellent verified effect.

Table 6. Comparison of main girder structural performance before and after optimization.

Performance Indicator	Original Design	Optimized Design	Improvement
Structural mass (t)	12.8	10.8	−15.6%
Max. equivalent stress (MPa)	186.7	171.2	−8.3%
Mid-span maximum deflection (mm)	48.5	43.2	−10.9%
First-order natural frequency (Hz)	2.45	2.75	+12.1%
Second-order natural frequency (Hz)	4.32	4.68	+8.3%
Structural compliance (J)	18.2	13.8	−24.2%
Maximum dynamic displacement (mm)	28.5	23.2	−18.6%
Dynamic stress concentration factor	1.47	1.32	−10.2%
Accumulated fatigue damage	0.89	0.73	−18.0%
Fatigue life (years)	~20	~23.7	+18.3%
Minimum safety factor	1.72	1.85	+7.6%
Material utilization rate (%)	71.2	84.6	+18.9%
Minimum wall thickness (mm)	8	8	Satisfies $\geq$ 6 mm

This synergistic improvement summarized in Table 5 is not coincidental but is a direct result of the multi-constraint optimization process. This is not simply minimization of mass. It searches for a material layout that simultaneously satisfies all imposed constraints. The 8.3% lesser maximum stress, and 10.9% lesser displacement with static loads are obtained because the process is driven to satisfy the stress and displacement constraints, and naturally ends up with the stiffer and more efficient layout. The 12.1% higher frequency is a direct result of the explicit frequency constraint. Most importantly, the improvement in the fatigue life is a result of the lesser peak stress and the improvement in the stress concentrations that are the initiators of fatigue cracks. Thus, each constraint has a meaningful impact on the solution, leading to an overall better design that is not just lighter, but better overall.

4. Conclusions and Outlook

4.1. Conclusions

Considering the engineering practicality inadequacy of the traditional lightweight design of gantry crane main girders, the presented article discussed multi-objective topology optimization design for gantry crane main girders with a variety of constraint factors. Such as static–dynamic performance, fatigue, minimum thickness of welded structure, etc., and established a three-objective optimization mathematical model, then an improved genetic algorithm was applied to solve its Pareto optimal solution. Sufficient static–dynamic mechanical performance verification was carried out. The research achievements show that the method can reduce the mass of the main girder by 15.6%, and improve the overall static–dynamic mechanical performance and fatigue life of the crane structure comprehensively. Also, the optimized result meets the requirement of manufacture and welding. The research contributes a viable technical method for lightweight design of the crane metal structure.

4.2. Limitations and Future Perspectives

This study has several limitations that point to future research directions. First, a linear elastic material model is employed, which neglects plastic deformation under extreme loading and may overestimate stiffness near the ultimate load. Second, welding residual stresses are not explicitly modeled, which could reduce effective fatigue life at weld joints. Third, manufacturing tolerances and geometric imperfections (e.g., initial web deflections, flange out-of-straightness) are not considered, potentially altering the stress distribution and load-carrying capacity. Fourth, the optimized design is validated solely through numerical simulation, without physical experimental testing, although the finite element model is verified through mesh independence and comparison with analytical solutions. Future work will address these limitations through high-fidelity nonlinear finite element models, welding residual stress simulation, probabilistic tolerance and imperfection analysis, and physical prototyping with static and dynamic testing. In addition, the manufacturability constraints can be expanded to include practical rules for weld layouts, assembly symmetry, and automated fabrication, and the proposed approach can be generalized to other engineering machinery components.

The proposed optimization framework is inherently modular and can be extended to other crane components and heavy machinery. For other crane components such as end carriages, trolley frames, support legs, and slewing platforms, the method is directly applicable by redefining the design domain, boundary conditions, and load spectra while retaining the same objective and constraint modules. For different types of heavy machinery, including bridge cranes, tower cranes, and port machinery (e.g., ship-to-shore and rubber-tired gantry cranes), the optimization loop remains valid; only the load cases and constraint thresholds need adjustment per the relevant design codes. The constraint modules for static strength, dynamic frequency, fatigue, and minimum weld thickness are independently configurable, and the modified genetic algorithm can be coupled with commercial finite element solvers through script interfaces to facilitate industrial adoption.

Furthermore, direct experimental validation of the optimized design is not included in this study. Full-scale experimental testing of a gantry crane girder requires substantial financial resources, specialized testing facilities, and strict safety protocols, which are beyond the scope of the current work. Instead, the finite element model is validated through: (1) comparison with analytical beam theory solutions, showing agreement

https://doi.org/10.3390/app16189064

within 5%; (2) comparison with published experimental data on similar crane girders; and (3) rigorous mesh independence verification. To address this limitation, future work will include: (1) fabrication of a scaled-down optimized girder specimen; (2) static loading tests to measure stress distribution and mid-span deflection; (3) experimental modal analysis using impact hammer testing to validate natural frequencies and mode shapes; and (4) comparison between experimental measurements and finite element predictions to quantify the accuracy of the numerical model.

Another future direction is extending the framework to evaluate structural behavior under fire exposure. Lightweight optimized structures with thinner sections may exhibit faster temperature rise and earlier strength degradation under fire conditions compared to conventional designs. Therefore, incorporating thermal-structural coupling analysis and fire resistance constraints into the optimization framework is essential to ensure structural integrity during fire events. In this context, thermal protection coatings for steel structures, such as the modified mortar coatings investigated in recent fire exposure studies [45], could complement the fire resistance of optimized lightweight steel structures. Integrating such thermal protection strategies with the proposed framework represents a promising research avenue.

Author Contributions: Conceptualization, Y.C. and J.T.; methodology, Y.C.; software, Y.C.; validation, Y.C. and J.T.; formal analysis, Y.C.; investigation, Y.C.; resources, J.T.; data curation, Y.C.; writing—original draft preparation, Y.C.; writing—review and editing, J.T.; visualization, Y.C.; supervision, J.T.; project administration, J.T.; funding acquisition, J.T. All authors have read and agreed to the published version of the manuscript.

Funding: This research received no external funding.

Institutional Review Board Statement: Not applicable.

Informed Consent Statement: Not applicable.

Data Availability Statement: All relevant data are available from the corresponding author upon reasonable request.

Conflicts of Interest: The authors declare no conflicts of interest.

Abbreviations

The following abbreviations are used in this manuscript:

SIMP	Solid Isotropic Material with Penalization
FEA	Finite Element Analysis
GA	Genetic Algorithm
MGA	Multi-objective Genetic Algorithm
VM	Von Mises
MS	Multi-objective Optimization
DOF	Degrees of Freedom

References

1. Hu, L.; Li, Y.; Zhang, G.Y.; Xiang, Y.J.; Zhang, Y.H. Topology optimization-based lightweight design of a certain tubular beam subframe. *J. Mech. Sci. Technol.* **2024**, *38*, 6253–6265. [CrossRef]
2. Sha, L.; Lin, A.; Zhao, X.; Kuang, S. A topology optimization method of robot lightweight design based on the finite element model of assembly and its applications. *Sci. Prog.* **2020**, *103*, 0036850420936482. [CrossRef] [PubMed]
3. Ma, H.; Wang, J.; Lu, Y.; Guo, Y. Lightweight design of turnover frame of bridge detection vehicle using topology and thickness optimization. *Struct. Multidiscip. Optim.* **2019**, *59*, 1007–1019. [CrossRef]
4. Xue, H.; Yu, H.; Zhang, X.; Quan, Q. A novel method for structural lightweight design with topology optimization. *Energies* **2021**, *14*, 4367. [CrossRef]

5. Zhang, S.; Li, H.; Huang, Y. An improved multi-objective topology optimization model based on SIMP method for continuum structures including self-weight. *Struct. Multidiscip. Optim.* **2021**, *63*, 211–230. [CrossRef]
6. Ahmed, F.; Deb, K.; Bhattacharya, B. Structural topology optimization using multi-objective genetic algorithm with constructive solid geometry representation. *Appl. Soft Comput.* **2016**, *39*, 240–250. [CrossRef]
7. Kunakote, T.; Bureerat, S. Multi-objective topology optimization using evolutionary algorithms. *Eng. Optim.* **2011**, *43*, 541–557. [CrossRef]
8. Sharma, S.K.; Sharma, R.C.; Lee, J. In situ and experimental analysis of longitudinal load on carbody fatigue life using nonlinear damage accumulation. *J. Damage Mech.* **2022**, *31*, 605–622. [CrossRef]
9. Wu, Z.; Fang, G.; Fu, M.; Chen, X.; Liang, J.; Lv, D. Random fatigue damage accumulation analysis of composite thin-wall structures based on residual stiffness method. *Compos. Struct.* **2019**, *211*, 546–556. [CrossRef]
10. Wang, J.; Li, Y.; Hu, G.; Yang, M. Lightweight research in engineering: A review. *Appl. Sci.* **2019**, *9*, 5322. [CrossRef]
11. Qi, Q.; Yu, Y.; Dong, Q.; Xu, G.; Xin, Y. Lightweight and green design of general bridge crane structure based on multi-specular reflection algorithm. *Adv. Mech. Eng.* **2021**, *13*, 16878140211051220. [CrossRef]
12. Hassan, H.Z.; Saeed, N.M. Advancements and applications of lightweight structures: A comprehensive review. *Discov. Civ. Eng.* **2024**, *1*, 47. [CrossRef]
13. Jang, I.G.; Kim, K.S.; Kwak, B.M. Conceptual and basic designs of the Mobile Harbor crane based on topology and shape optimization. *Struct. Multidiscip. Optim.* **2014**, *50*, 505–515. [CrossRef]
14. Yue, P.; Ma, J.; Zhou, C.; Jiang, H.; Wriggers, P. A fatigue damage accumulation model for reliability analysis of engine components under combined cycle loadings. *Fatigue Fract. Eng. Mater. Struct.* **2020**, *43*, 1880–1892. [CrossRef]
15. Tong, Y.; Ye, W.; Yang, Z.; Li, D.; Li, X. Research on multidisciplinary optimization design of bridge crane. *Math. Probl. Eng.* **2013**, *2013*, 763545. [CrossRef]
16. Li, A.; Liu, C. Lightweight design of a crane frame under stress and stiffness constraints using super-element technique. *Adv. Mech. Eng.* **2017**, *9*, 1687814017716621. [CrossRef]
17. Simonetti, H.L.; Almeida, V.S.; das Neves, F.A.; Greco, M. Multi-objective topology optimization using the boundary element method. *Structures* **2019**, *19*, 84–95. [CrossRef]
18. Marck, G.; Nemer, M.; Harion, J.L.; Russeil, S.; Bougeard, D. Topology optimization using the SIMP method for multiobjective conductive problems. *Numer. Heat Transf. Part B Fundam.* **2012**, *61*, 439–470. [CrossRef]
19. Deng, J.; Yan, J.; Cheng, G. Multi-objective concurrent topology optimization of thermoelastic structures composed of homogeneous porous material. *Struct. Multidiscip. Optim.* **2013**, *47*, 583–597. [CrossRef]
20. Zhou, X.; Bai, Y.; Nardi, D.C.; Russeil, S.; Bougeard, D. Damage evolution modeling for steel structures subjected to combined high cycle fatigue and high-intensity dynamic loadings. *Int. J. Struct. Stab. Dyn.* **2022**, *22*, 2240012. [CrossRef]
21. Hiep, V.D.; Quynh, N.X.; Tung, T.T. A topology optimization design of a crane hook. *Results Eng.* **2024**, *23*, 102492. [CrossRef]
22. Shen, H.; Wei, L.; Zhang, T.; Zhang, X.; Zheng, Z.; Han, E.; Li, S. Research on lower limb lightweight of bionic robot based on lattice structure unit. *Sci. Rep.* **2025**, *15*, 29316. [CrossRef] [PubMed]
23. Huang, D.; Zhou, S.; Yan, X. Multi-objective topology optimization design of thermal-mechanical coupling structure based on FPTO method. *Optim. Eng.* **2025**, *26*, 53–81. [CrossRef]
24. Zhou, Y.; Nomura, T.; Zhao, E.; Saitou, K. Large-scale three-dimensional anisotropic topology optimization of variable-axial lightweight composite structures. *J. Mech. Des.* **2022**, *144*, 011702. [CrossRef]
25. Liu, J.; Zhu, N.; Chen, L.; Liu, X. Structural multi-objective topology optimization in the design and additive manufacturing of spatial structure joints. *Int. J. Steel Struct.* **2022**, *22*, 649–668. [CrossRef]
26. Al Ali, M.; Sahib, A.Y.; Al Ali, M. Teeth implant design using weighted sum multi-objective function for topology optimization and real coding genetic algorithm. In Proceedings of the 6th IIAE International Conference on Industrial Application Engineering, Tokyo, Japan, 24 March 2018.
27. Suvorov, V.; Vasilyev, R.; Melnikov, B.; Kuznetsov, I.; Bahrami, M.R. Weight reduction of a ship crane truss structure made of composites. *Appl. Sci.* **2023**, *13*, 8916. [CrossRef]
28. Wang, F.Y.; Xu, Y.L.; Sun, B.; Zhu, Q. Dynamic stress analysis for fatigue damage prognosis of long-span bridges. *Struct. Infrastruct. Eng.* **2019**, *15*, 582–599. [CrossRef]
29. Lin, J.; Luo, Z.; Tong, L. A new multi-objective programming scheme for topology optimization of compliant mechanisms. *Struct. Multidiscip. Optim.* **2010**, *40*, 241–255. [CrossRef]
30. Sun, B.; Zhu, Z.; Shi, C.; Luo, Z. Dynamic mechanical behavior and fatigue damage evolution of sandstone under cyclic loading. *Int. J. Rock Mech. Min. Sci.* **2017**, *94*, 82–89. [CrossRef]
31. Zhou, X.; Zhang, D.; Nowamooz, H.; Jiang, C.; Ye, C. Investigation on damage and failure mechanisms of roadway surrounding rock triggered by dynamic–static combined loads. *Rock Mech. Rock Eng.* **2022**, *55*, 5639–5657. [CrossRef]
32. Modrek, M.; Viswanath, A.; Khan, K.A.; Ali, M.I.H.; Abu Al-Rub, R.K. Multi-objective topology optimization of passive heat sinks including self-weight based on triply periodic minimal surface lattices. *Case Stud. Therm. Eng.* **2023**, *42*, 102684. [CrossRef]

33. Wang, G.; Zhu, D.; Liu, N.; Zhao, W. Multi-objective topology optimization of a compliant parallel planar mechanism under combined load cases and constraints. *Micromachines* **2017**, *8*, 279. [CrossRef] [PubMed]
34. Kenan, H.; Azeloğlu, C.O. Experimental Modal Analysis Assessment of a Scaled-Down Tower Crane Mast to be Used in Experimental Studies. *Iran. J. Sci. Technol. Trans. Mech. Eng.* **2023**, *47*, 1867–1876. [CrossRef]
35. Liu, Z.; Liu, C.; He, Z.; Gan, Y.; Li, B. Analysis of Coupled Vibration and Swing Characteristics of Bridge Crane. In Proceedings of the Journal of Physics: Conference Series, Online, 20 September 2021.
36. Wu, J.J. Finite element analysis and vibration testing of a three-dimensional crane structure. *Measurement* **2006**, *39*, 740–749. [CrossRef]
37. Cheng, B.; Yang, B.; Wang, D.; Duan, M. Finite element analysis of complete structure of tower cranes. In Proceedings of the Journal of Physics: Conference Series, Online, 15 May 2023.
38. Hamad, A.G.; Aswed, K.K.; Al Rjoub, Y.; Firouzi, N.; Podulka, P. Nonlinear Deformation Analysis of Sandwich Timoshenko Beams with Carbon Nanotube Reinforced Face Sheets and Re-Entrant Core Using GDQ Method. *Mathematics* **2026**, *14*, 630. [CrossRef]
39. Altaee, M.K.; Hamad, A.G.; Alhussein, T.H.; Al Rjoub, Y.S.; Firouzi, N.; Podulka, P. Nonlinear Vibration of Temperature-Dependent FGM Beams with Symmetric and Asymmetric Boundary Conditions via the Generalized Differential Quadrature Method. *Computation* **2026**, *14*, 113. [CrossRef]
40. Liu, K.; Yeoh, K.M.; Cui, Y.; Zhao, A.; Luo, Y.; Zhong, Z. Integrated multiscale topology optimization of frame structures for minimizing compliance. *Eng. Struct.* **2025**, *339*, 120561. [CrossRef]
41. Jia, F.; Gao, P.; Mo, A. Consider the Multi-Objective Topology Optimization Design of a Space Structure Under Complex Working Conditions. *Mathematics* **2025**, *13*, 2133. [CrossRef]
42. Fang, Z.; Yang, L.; Du, D.; He, K.; Zhu, D.; Zhang, Y. Study on multi-objective topology optimization design for support structure. In Proceedings of the 2010 International Conference on Mechanic Automation and Control Engineering, Wuhan, China, 26 June 2010.
43. Bendsøe, M.P.; Sigmund, O. *Topology Optimization: Theory, Methods and Applications*; Springer: Berlin, Germany, 2003.
44. Sigmund, O. A 99 line topology optimization code written in Matlab. *Struct. Multidiscip. Optim.* **2001**, *21*, 120–127. [CrossRef]
45. Bolina, F.L.; Henn, A.S.; Silva, D.B.; Pachla, E.C. Numerical Evaluation of Modified Mortar Coatings for Thermal Protection of Reinforced Concrete and Steel Structures Under Standardized Fire Exposure. *Coatings* **2025**, *15*, 806. [CrossRef]

https://doi.org/10.3390/app16189064